Chemical Science

ROYAL SOCIETY OF CHEMISTRY

EDGE ARTICLE

View Article Online
View Journal | View Issue

Cite this: *Chem. Sci.*, 2024, **15**, 6833

All publication charges for this article have been paid for by the Royal Society of Chemistry

Regulating electron transfer and orbital interaction within metalloporphyrin-MOFs for highly sensitive NO_2 sensing†

Er-Xia Chen,[ab] Liang He,[a] Mei Qiu,*[c] Yongfan Zhang,[d] Yayong Sun,[a] Wen-Hua Li,[a] Jian-Ze Xiao,[a] Jie Chen,[a] Gang Xu *[abe] and Qipu Lin *[aef]

The understanding of electron transfer pathways and orbital interactions between analytes and adsorption sites in gas-sensitive studies, especially at the atomic level, is currently limited. Herein, we have designed eight isoreticular catechol–metalloporphyrin scaffolds, FeTCP–M and InTCP–M (TCP = 5,10,15,20-tetrakis-catechol-porphyrin, M = Fe, Co, Ni and Zn) with adjustable charge transfer schemes in the coordination microenvironment and precise tuning of orbital interactions between analytes and adsorption sites, which can be used as models for exploring the influence of these factors on gas sensing. Our experimental findings indicate that the sensitivity and selectivity can be modulated using the type of metals in the metal–catechol chains (which regulate the electron transfer routes) and the metalloporphyrin rings (which fine-tune the orbital interactions between analytes and adsorption sites). Among the isostructures, InTCP–Co demonstrates the highest response and selectivity to NO_2 under visible light irradiation, which could be attributed to the more favorable transfer pathway of charge carriers in the coordination microenvironment under visible light illumination, as well as the better electron spin state compatibility, higher orbital overlap and orbital symmetry matching between the N-2s2p$_z$ hybrid orbital of NO_2 and the Co-3d$_{z^2}$ orbital of InTCP–Co.

Received 23rd December 2023
Accepted 19th March 2024

DOI: 10.1039/d3sc06909e

rsc.li/chemical-science

Introduction

Understanding the atomic-scale sensing nature is essential for enhancing performance and gaining mechanistic insight into responses of analytes. Specifically, charge transfer during the gas sensing process and the interactions between analytes and adsorption sites at the atomic-level are fundamental factors in causing signal changes in gas induction.[1,2] Although a variety of gas sensitive materials, such as semiconducting metal oxides,[3–5] metal dichalcogenides,[6,7] graphene-based hybrids,[8,9] and conducting polymers,[10,11] have attracted significant attention in the past few decades, their ambiguous structures or adsorption sites have limited the comprehension of the reaction processes between gas-sensitive materials and analytes at the atomic level, including electron transfer routes, electron spin states and orbital symmetry/overlap between adsorbates and adsorption sites, all of which have a microregulatory on gas-sensitive properties.

As one of the emerging sensing materials, metal–organic frameworks (MOFs) might be promising platforms to address the issues because of their inherent features, such as well-defined and tailorable structures, accessible adsorption sites, high porosity and substantial surface areas.[12–17] In line with our discovery in 2014 that ZIF-67 and $[Co(im)_2]_n$ have chemiresistive behavior in detecting formaldehyde and trimethylamine,[18,19] several chemiresistive sensors based on pure-MOFs have been developed.[20–25] For instance, Kalidindi *et al.* utilized an amine-modified Zr-based MOF, NH_2–UiO-66, to detect acidic gases (*i.e.*, SO_2, NO_2 and CO_2) at the parts-per-million (ppm) level.[26] Dincă *et al.* investigated a two-dimensional (2D) MOF, Cu_3(-HITP)$_2$ (HITP = 2,3,6,7,10,11-hexaiminotriphenylene), with high electrical conductivity and a detection limit of less than ppm (sub-ppm) for NH_3 vapor.[27] Zuo *et al.* synthesized a series of mixed-linker MOFs, which demonstrated adjustable sensing performance for volatile organic compounds (VOCs) by varying the ratio of mixed-linkers.[28] In our research, we fabricated a chemiresistive heterostructured MOF-based sensor by integrating two types of MOF layer, achieving high selectivity

[a]State Key Laboratory of Structural Chemistry, Fujian Provincial Key Laboratory of Materials and Techniques toward Hydrogen Energy, Fujian Institute of Research on the Structure of Matter, Chinese Academy of Sciences, Fuzhou, Fujian 350002, China. E-mail: gxu@fjirsm.ac.cn; linqipu@fjirsm.ac.cn

[b]Fujian Science & Technology Innovation Laboratory for Optoelectronic Information of China, Fuzhou, Fujian 350108, China

[c]College of Chemistry and Materials, Jiangxi Agricultural University, Nanchang, Jiangxi 330045, China. E-mail: qium@jxau.edu.cn

[d]College of Chemistry, Fuzhou University, Fuzhou, Fujian 350116, China

[e]University of Chinese Academy of Sciences, Beijing 100049, China

[f]State Key Laboratory of Photocatalysis on Energy and Environment, Fuzhou University, Fuzhou, Fujian 350116, China

† Electronic supplementary information (ESI) available. See DOI: https://doi.org/10.1039/d3sc06909e

and response to benzene at room temperature.[29] Although MOFs have shown potential as sensitive materials for chemiresistive sensors, their interactions with gas (vapor) and the effect of charge transfer routes within MOFs during gas-sensing, particularly at the atomic-level, remain unclear. Consequently, it is still required to explore the influence of these factors on gas-sensitive properties by designing suitable MOFs.

The indirect (and direct) band gaps of typical semiconducting hematite (α-Fe_2O_3) and cubic indiumtrioxide (c-In_2O_3) are ~2.1 eV (~3.3 eV) and ~2.8 eV (>3.5 eV), respectively (Fig. 1a–f).[30–33] In the structures of α-Fe_2O_3 and c-In_2O_3, both Fe and In adopt six-coordination patterns to form 1D Fe^{3+}–oxo or In^{3+}–oxo chains. These chains are fused to produce 3D structures with the help of μ_4-O moieties (Fig. 1a, b and d–f).[34,35] Meanwhile, metalloporphyrins have gained much attention in the fields of molecular recognition, gas sensing and catalysis due to their open and adjustable metal sites in the porphyrin plane and excellent light absorption.[36–39] Inspired by the difference in band gaps (especially the indirect band gaps) and structural features of α-Fe_2O_3/c-In_2O_3 and the characteristics of metalloporphyrins, assembling In^{3+}/Fe^{3+}–oxo chains and suitable metalloporphyrin ligands into MOFs might offer a platform for exploring the effect of electron transfer paths within MOFs and orbital interactions between analytes and adsorption sites during the gas response.

Under the guidance of theoretical simulation and calculation, we designed a series of isoreticular metalloporphyrinic metal–catechol (MPMC) scaffolds, FeTCP–M and InTCP–M, which feature In^{3+}/Fe^{3+}–oxo chains connected by catechol–metalloporphyrin arrays (Fig. 1g–j, where TCP = 5,10,15,20-tetrakis-catechol-porphyrin and M = Fe, Co, Ni, and Zn), to investigate the influence of electron transfer routes within MOFs and orbital interactions between analytes and adsorption sites on the overall chemiresistive sensing. Remarkably, we discovered that the sensing capability for NO_2 can be efficiently tuned by regulating the metal types in both the metal–oxo chains and the porphyrin planes. Among these isomorphic scaffolds, InTCP–Co exhibited the highest response and selectivity toward NO_2. This was attributed to several factors, including the impact of visible light absorption, the preferable electron transfer routes, a higher orbital overlap and suitable matching of the orbital symmetry and electron spin state between the N-2s2p_z hybrid orbital of NO_2 and the Co-3d_{z^2} orbital of InTCP–Co.

Results and discussion

FeTCP–M and InTCP–M (M = Fe, Co, Ni, and Zn) were prepared using the solvothermal method, as detailed in the ESI (Sections S2 and S3†). Refinement of experimentally obtained high-resolution PXRD patterns (Fig. S1–S4†) established their isostructures.[40] These structures consist of infinite In^{3+}/Fe^{3+}–oxo chains that are connected by eclipsed catechol–metalloporphyrin arrays (Fig. 1g–j). By manipulating the metal nodes in the metal–catechol rods, the energy band structures can be varied, which potentially influence electron transfer patterns and subsequently modulate the properties.[23,27,40–44] Removal of the coordinated molecules in the axial direction leads to a planar tetragonal coordination geometry for the metals (Fe, Co, Ni and Zn) centered in the porphyrin rings (Fig. 1i). The different metal types in the porphyrin rings have distinct electron configurations, which could regulate the interactions

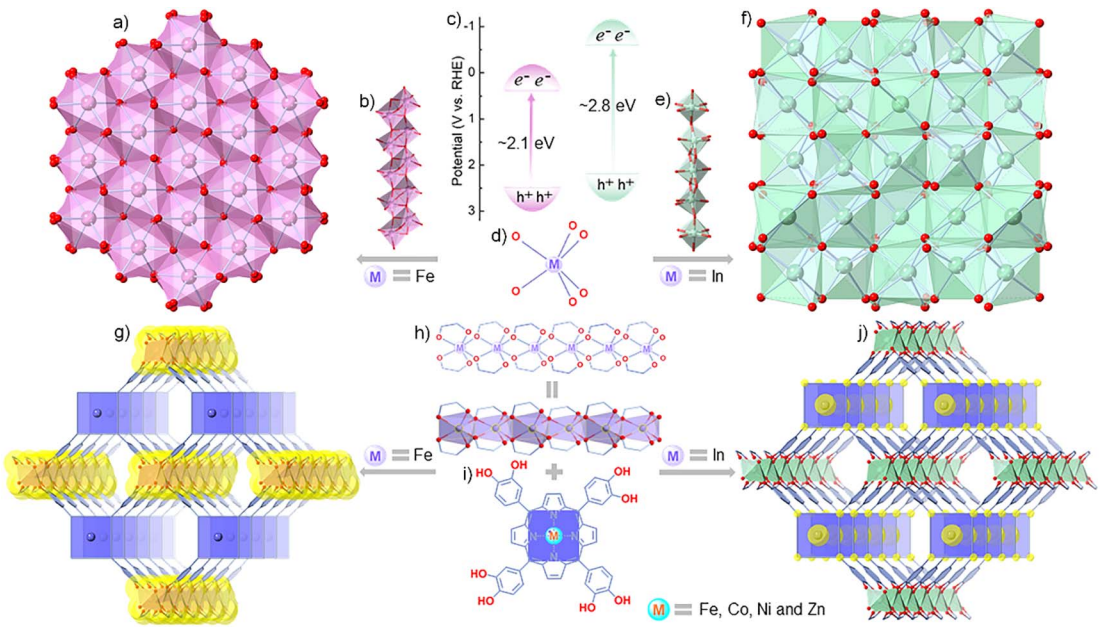

Fig. 1 (a) The structure of α-Fe_2O_3; (b) the Fe–O chain in α-Fe_2O_3; (c) the schematic illustration of the indirect band gaps of α-Fe_2O_3 and c-In_2O_3; (d) the coordination configuration of Fe in α-Fe_2O_3 and In in c-In_2O_3; (e) the In–O chain in c-In_2O_3; (f) the structure of c-In_2O_3; (g) the 3D structure of FeTCP–M; (h) In/Fe–catechol coordination chains; (i) catechol–metalloporphyrin ligand; (j) the 3D structure of InTCP–M; all H atoms are omitted for clarity, M = Fe, Co, Ni and Zn.

between (In/Fe)TCP–M (M = Fe, Co, Ni and Zn) and analytes, thereby tuning the properties.[45–47] Scanning electron microscopy (SEM) revealed a nanoplate-like grain morphology for (In/Fe)TCP–M (Fig. S5 and S6†). The microporous nature of (In/Fe)TCP–M was confirmed by N_2 adsorption–desorption isotherms at 77 K (Fig. S7–S10†). The Brunauer–Emmett–Teller (BET) and Langmuir surface areas and pore size distribution are presented in Table S1.† As shown in Fig. S11 and S12,† the UV/vis diffuse reflectance spectra (DRS) of (In/Fe)TCP–M demonstrated a broad range of light absorption from 250 to 800 nm, indicating that they can easily generate photogenerated charge carriers under visible-light illumination.

The well-defined chemical structure, regulated electronic structure, high porosity and gas uptake, and excellent visible light absorption make FeTCP–M and InTCP–M (M = Fe, Co, Ni, and Zn) suitable models for exploring the effect of charge transfer routes within MOFs and orbital interactions between adsorbates and adsorption sites on the chemiresistive sensing performance under visible light irradiation. Experimentally, FeTCP–M and InTCP–M (M = Fe, Co, Ni, and Zn) powders were individually coated on interdigital electrodes and used as sensitive devices (Fig. S13a†). The gas-sensing measurements were conducted using a custom-built instrument with a dynamic gas distribution system (Fig. S13b†), where the current of the devices in various gaseous analytes was monitored using a source meter (the details are in the Methods).

The real-time gas-sensing curves of FeTCP–M and InTCP–M (M = Fe, Co, Ni and Zn) showed different response values to 10 ppm NO_2 at room temperature under visible-light irradiation (Fig. 2a). FeTCP–M (M = Fe, Co, Ni and Zn) demonstrated response values of 179%, 156%, 163% and 160%, respectively (Fig. 2a), indicating that the metal types in the porphyrin rings exerted no significant influence on the response values for FeTCP–M. In contrast, the response values of InTCP–M were substantially affected by the metal types in the porphyrin rings, resulting in response values of 426%, 937%, 187% and 172% for M = Fe, Co, Ni and Zn, respectively (Fig. 2a). Notably, InTCP–M demonstrated a higher response value to 10 ppm NO_2 compared to FeTCP–M with identical metal types in the porphyrin rings, suggesting their different sensing mechanisms. Among FeTCP–M and InTCP–M (M = Fe, Co, Ni and Zn), InTCP–Co displayed the highest response value. Recycling experiments of the real-time sensing curves for 10 ppm NO_2 were conducted to evaluate the stability and repeatability of (In/Fe)TCP–M. Their initial response values were maintained in six successive assays, demonstrating good stability and repeatability (Fig. 2b and S14–S20†).

NO_2 concentration (40 ppb to 100 ppm) dependent responses of InTCP–Co are presented in Fig. 2c, where InTCP–Co exhibits excellent response/recovery performance over a wide range of NO_2 concentrations. The corresponding plot of response *vs.* concentration of InTCP–Co towards NO_2 displays a good linear relationship ($R^2 = 0.982$, Fig. 2d) within the range of 40 ppb to 10 ppm. Fig. S21† shows that InTCP–Co has a response time of 3.8 min and a recovery time of 13.1 min when exposed to 10 ppm NO_2. The relatively long recovery time may be caused by the relatively strong affinity between NO_2 and InTCP–Co. To assess the anti-interference performance of the InTCP–Co sensor in practical applications, the selectivity of InTCP–Co was further evaluated by examining the response of the sensor to various interfering gases at 100 ppm, including ammonia (NH_3), methylamine (CH_3NH_2), carbon dioxide (CO_2), carbon monoxide (CO), nitric oxide (NO), hydrogen sulfide (H_2S), methane (CH_4), ethylene (C_2H_4), methanol (CH_3OH), and benzene (C_6H_6). As shown in Fig. 2e, compared with NO_2, the response values of the interfering gases were negligible. Further

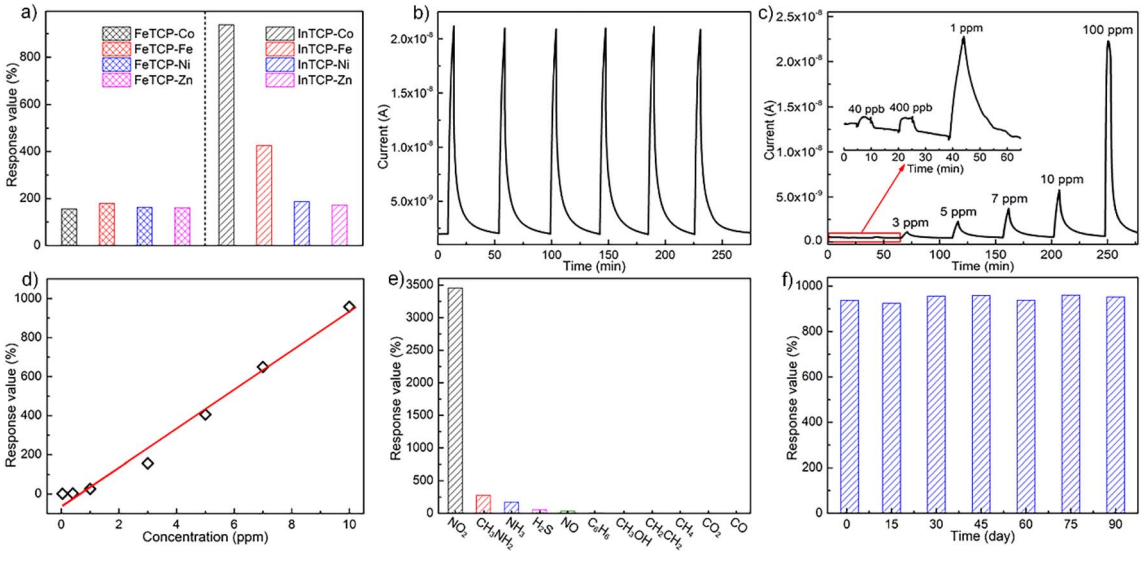

Fig. 2 (a) The response values of FeTCP–M and InTCP–M sensors (M = Fe, Co, Ni and Zn) to 10 ppm NO_2; (b) the dynamic response–recovery curve of InTCP–Co to 10 ppm NO_2 with six consecutive cycles; (c) the dynamic response–recovery curve of InTCP–Co to NO_2 at different concentrations; (d) the plot of response value-concentration of InTCP–Co to NO_2; (e) the response values of InTCP–Co to different interfering gases; (f) the stability of InTCP–Co to 10 ppm NO_2 in 90 days.

experiments showed that InTCP–Co could still distinguish NO_2 when NO_2 was mixed with other gases (Fig. S22†), confirming that InTCP–Co possesses excellent selectivity.

Additional reference experiments were conducted at different temperatures without visible light irradiation. The response of InTCP–Co to 10 ppm NO_2 was notably ineffective (Fig. S23–S28†), suggesting that visible photo-induced charge carriers can improve gas sensing properties, whereas temperature has a negligible effect on gas sensitivity. When the catechol–metalloporphyrin ligand (3,4-TDHPP–Co) was used as the sensing material, the response value to 10 ppm NO_2 was only 53% under the same operating conditions (Fig. S29 and S30†). This finding indicates that assembling 3,4-TDHPP–Co into the porous MOFs can effectively enhance gas sensitivity. Moreover, after three months, the original response value of InTCP–Co towards 10 ppm NO_2 was retained as demonstrated in Fig. 2f. The PXRD patterns in Fig. S31† also illustrate the structural integrity of InTCP–Co and its excellent long-term stability as a sensor. These features indicate that InTCP–Co is a good sensing material for NO_2 at room temperature and under visible light irradiation (Table S2†).

To unveil the impact of substitutable metal species in the porphyrin rings and 1D coordination nodes on gas sensing properties, we resorted to DFT calculations. The optimal configurations for NO_2 adsorption on FeTCP–M and InTCP–M (M = Fe, Co, Ni and Zn) are presented in Fig. S39 and S40.† NO_2 molecules are adsorbed on the metals in the porphyrin rings in a V-shape configuration. It can be seen from the charge difference density maps (Fig. 3a and S41–S44†) that the charge density distributions are different between NO_2 and the adsorption sites of FeTCP–M and InTCP–M (M = Fe, Co, Ni and Zn), indicating distinct interactions between NO_2 and (In/Fe)TCP–M (M = Fe, Co, Ni and Zn). We further confirmed the different interplay between NO_2 and (In/Fe)TCP–M (M = Fe, Co, Ni and Zn) by N 1s XPS spectroscopy (Fig. 3b and S32–S38†). After NO_2 capture, two new peaks appear at approximately 405.2 and 406.5 eV, respectively, when compared to (In/Fe)TCP–M (M = Fe, Co and Ni) prior to the NO_2 response (Fig. 3b, S32, S33 and S35–S37†). The peak at a lower bonding energy (~405.2 eV) was assigned to NO_2^- species and the peak at a higher bonding energy (~406.5 eV) was ascribed to NO_3^- species or NO_2 (N_2O_4) chemisorbed on (In/Fe)TCP–M (M = Fe, Co and Ni) in the molecular form,[48–50] which is consistent with *in situ* diffuse reflectance infrared Fourier-transform spectroscopy (DRIFT, Fig. 3c). The emerging bands at 1207 and 1480 cm^{-1} belong to NO_2^- species.[51–53] The bands at 1218, 1248 and 1306 cm^{-1} are assigned to NO_3^- species.[51,54] However, no obvious changes were observed in the N 1s XPS spectra of (In/Fe)TCP–Zn before and after NO_2 sorption (Fig. S34 and S38†), suggesting that the interactions between NO_2 and (In/Fe)TCP–Zn were weaker than those between NO_2 and (In/Fe)TCP–M (M = Fe, Co and Ni).

To further explore the different interactions between NO_2 and (In/Fe)TCP–M (M = Fe, Co, Ni and Zn), we analyzed the density of states (DOS) of the MPMC scaffolds before and after NO_2 capture. As shown in Fig. 4a, there are no significant changes in the total density of states (TDOS) near the Fermi level of FeTCP–M (M = Fe, Co, Ni and Zn) before and after NO_2 sorption, indicating the weak orbital interactions between NO_2 and the main orbital compositions near the Fermi level. However, the TDOS of InTCP–M (M = Fe, Co, Ni and Zn) show marked differences before and after NO_2 sorption when changing the metal types in porphyrin rings (Fig. 4b). The TDOS of InTCP–Zn remain essentially unchanged, indicating weak orbital interaction between NO_2 and the major orbital compositions near the Fermi level of InTCP–Zn. This might be mainly attributed to the full occupation of Zn-3d orbitals. The changes in the TDOS are substantial for InTCP–M (M = Fe, Co, Ni) before and after NO_2 capture, especially around the Fermi level, indicating that the orbital interactions between NO_2 and the dominant orbital components near the Fermi level of InTCP–M (M = Fe, Co, Ni) are stronger.

The projected density of states (PDOS) of InTCP–M after NO_2 adsorption demonstrates that the orbital interactions between NO_2 and InTCP–M mainly derive from the sp^2 hybrid orbital of NO_2 and the M-3d_{z^2} orbitals of InTCP–M (M = Fe, Co and Ni, Fig. 4c, d and S45–S48†). Further analysis shows that the M-3d_{z^2} orbitals interacting with NO_2 stem from the beta states (M = Fe, Co and Ni, Fig. 4e, f, S45 and S46†). The crystal orbital overlap population (COOP) is widely used to understand the bonding and antibonding contributions of interacting components and its integrated value (ICOOP) could reflect the strength of the interaction.[55,56] It can be seen from Table S3† that the interaction between beta states of electron spin in M-3d_{z^2} and NO_2 follows the order: InTCP–Co > InTCP–Fe > InTCP–Ni > InTCP–Zn, in line with the sensitive response to NO_2 under visible light irradiation. Compared with visible light illumination, the temperature does

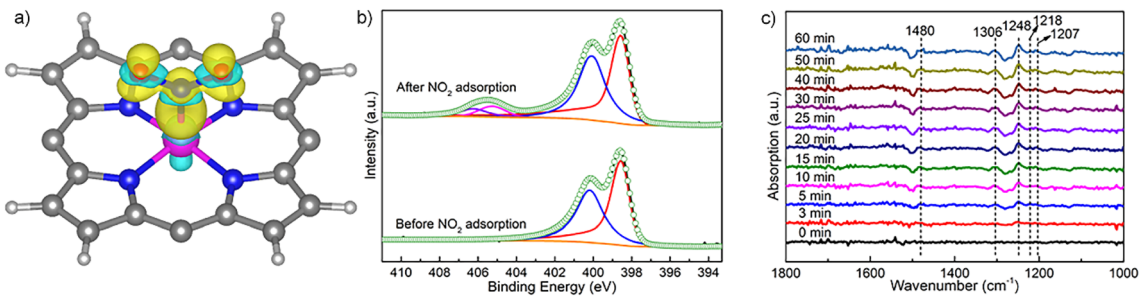

Fig. 3 (a) The charge difference density map of NO_2 affined on InTCP–Co (the other parts of the structure of InTCP–Co have been omitted for clarity); (b) the N 1s XPS spectra of InTCP–Co before and after the NO_2 response; (c) the *in situ* DRIFT spectra of InTCP–Co in a 100 ppm NO_2 atmosphere.

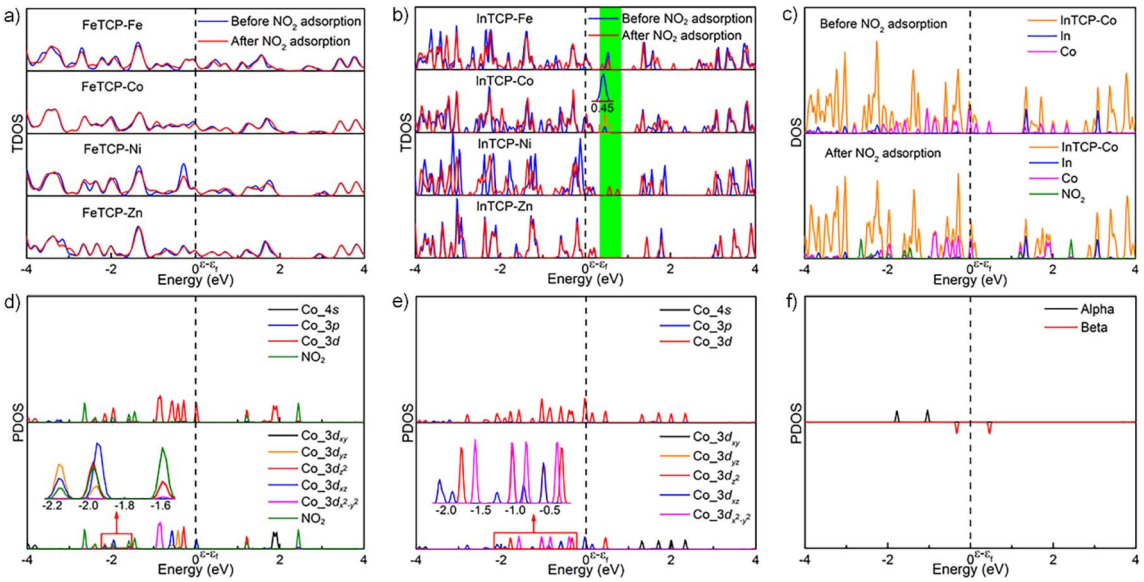

Fig. 4 The TDOS of (a) FeTCP–M and (b) InTCP–M before and after the NO_2 response (M = Fe, Co, Ni and Zn); (c) the TDOS and PDOS of InTCP–Co before and after the NO_2 response; (d) the PDOS of NO_2 and Co-4s, Co-3p, Co-3d orbitals of InTCP–Co after the NO_2 response; (e) the PDOS of Co-4s, Co-3p and Co-3d orbitals of InTCP–Co before the NO_2 response; (f) the PDOS of electron spin states in the Co-$3d_{z^2}$ orbital of InTCP–Co.

not significantly affect the sensitive response to NO_2 for InTCP–Co. The reason may be that visible light can conduce to produce photogenerated electrons, which can then jump into the unoccupied Co-$3d_{z^2}$ orbitals, thereby enhancing the orbital interaction between NO_2 and InTCP–Co to improve the sensitive response to NO_2. But photoelectrons could not be produced under the dark conditions or by heating. Therefore, the visible-light-driven sensitive response to NO_2 is higher than that in the dark or at different temperatures. Although the PDOS of FeTCP–M after NO_2 adsorption also manifests that the orbital interactions between NO_2 and FeTCP–M originate from the beta state of electron spin in the M-$3d_{z^2}$ orbitals (M = Fe, Co, and Ni, Fig. S51–S54†), the ICOOP values of the beta state of electron spin in M-$3d_{z^2}$ orbitals and NO_2 are different (Table S3†). It can be seen from the PDOS of FeTCP–M (M = Fe, Co, Ni and Zn, Fig. S49 and S50†) that the photoelectrons primarily transfer to the Fe–oxo chains. Hence, the sensitive response to NO_2 with the same concentrations does not exhibit a notable difference under the visible-light excitation for FeTCP–M (M = Fe, Co, Ni and Zn). This indicates that the degree of orbital overlap, the electron spin state in the orbital, the electron transfer routes in the microenvironment within a MOF and visible light irradiation have a significant influence on the sensitive response to NO_2.

To reveal the selectivity of InTCP–Co to various analytes, we conducted calculations to determine the optimal adsorption configurations for ten typical interfering gases on InTCP–Co (Fig. S55 and S56†). It can be seen that, C_6H_6, CH_4 and CO_2 were not adsorbed on InTCP–Co in the optimal adsorption configuration, suggesting that the interactions between InTCP–Co and $C_6H_6/CH_4/CO_2$ are weak individually. It was further confirmed by the adsorption energies (E_{ads}) and the DOS of InTCP–Co after C_6H_6, CH_4 and CO_2 interaction (Table S4 and Fig. S57–S61†). The weak affinities between InTCP–Co and $C_6H_6/CH_4/CO_2$ cannot cause changes in the structure or the local electron/hole concentrations in InTCP–Co. Therefore, InTCP–Co shows negligible response values for $C_6H_6/CH_4/CO_2$. Except for C_6H_6, CH_4 and CO_2, the other seven typical interfering gases could be adsorbed on InTCP–Co. However, their adsorption energies are diverse, indicating that the interactions between these analytes and InTCP–Co are different. Among all of the measured analytes, InTCP–Co possesses the most negative energy (−3.08 eV) for the NO_2 response, indicating that the interaction between NO_2 and InTCP–Co is stronger than that of other analytes measured. The DOS of InTCP–Co after adsorbing diverse analytes (NO_2, CH_3NH_2, NH_3, H_2S, NO, CH_3OH, CH_2CH_2 and CO) have changed differently (Fig. 4c, d and S62–S68†), which further indicates the distinctive orbital interactions between diverse analytes and InTCP–Co.

To investigate the inherent essence of the different orbital interactions between the adsorbed analytes and Co in the porphyrin ring of InTCP–Co, further analyses have been performed using the PDOS associated with the crystal orbital Hamilton populations (COHP)[57–59] and natural bond orbital (NBO).[60,61] It is well known that there are unpaired electrons in free NO_2 and NO molecules. The electrons in CH_3NH_2, NH_3, CO, H_2S, CH_3OH, and C_2H_4 in their free states are all paired. As shown in Fig. 5a, the redistributed PDOS of N in NO_2 and Co in InTCP–Co are overlapped and changed upon trapping NO_2 into InTCP–Co, demonstrating that orbital hybridization interaction occurs between Co in InTCP–Co and N in NO_2. To further disclose the origin of the orbital hybridization between N in NO_2 and Co in InTCP–Co, we examined the COHP curve of Co–N. The COHP curve clearly indicates that the orbital hybridization is driven by the Co-$3d_{z^2}$ and N-2s2p_z hybrid orbitals (Fig. 5a)

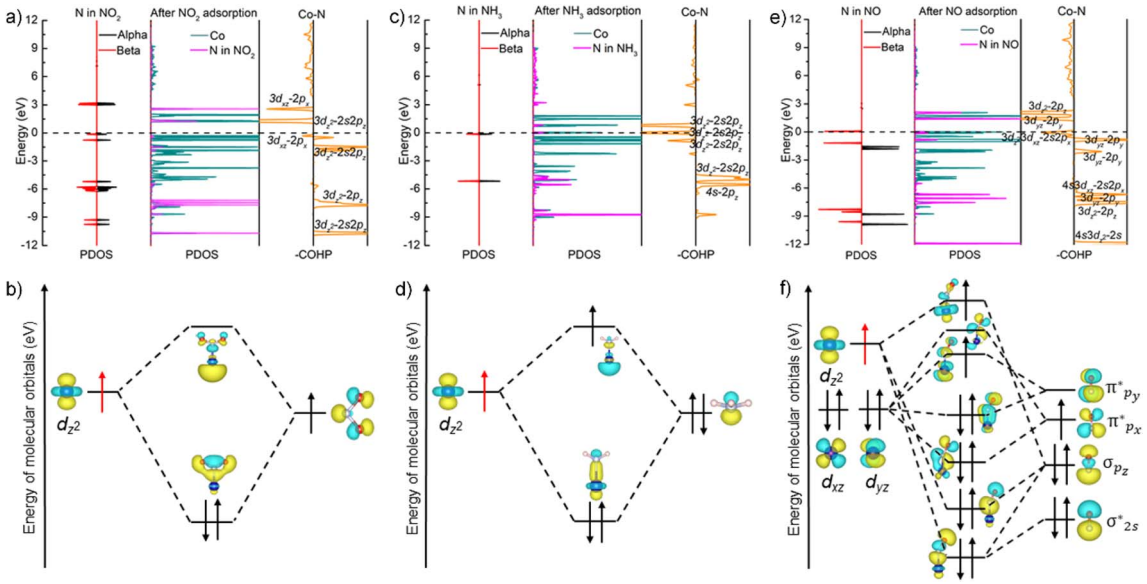

Fig. 5 (a) The PDOS patterns of N in NO_2 in the free state, Co in InTCP–Co and N in NO_2 after the NO_2 response, and the COHP curve of the Co–N bond between Co in InTCP–Co and N in NO_2 after the NO_2 response; (b) the dominant interaction and the energy levels of the scalar relativistic Kohn–Sham molecular orbitals of InTCP–Co after NO_2 adsorption with correlation with the orbitals from Co-3d_{z^2} and NO_2; (c) the PDOS patterns of N in NH_3 in the free state, Co in InTCP–Co and N in NH_3 after the NH_3 response, and the COHP curve of the Co–N bond between Co in InTCP–Co and N in NH_3 after the NH_3 response; (d) the major interaction and the energy levels of the scalar relativistic Kohn–Sham molecular orbitals of InTCP–Co after the NH_3 response with correlation with the orbitals from Co-3d_{z^2} and NH_3; (e) the PDOS patterns of N in NO in the free state, Co in InTCP–Co and N in NO after the NO response, and the COHP curve of the Co–N bond between Co in InTCP–Co and N in NO after the NO response; (f) the main interaction and energy levels of the scalar relativistic Kohn–Sham molecular orbitals of InTCP–Co after the NO response with correlation with the orbitals from Co-3d_{z^2} and NO; the electron in Co-3d_{z^2} orbital derives from photogenerated electrons in (b), (d) and (f).

which display a bonding character, indicating the presence of a relatively strong orbital interaction between N in NO_2 and Co in InTCP–Co. Additionally, the NBO analysis is employed to further visualize the orbital hybridization interaction. As shown in Fig. 5b, the symmetrical N-2s2p_z hybrid orbital occupied by one electron in NO_2 hybridizes with the Co-3d_{z^2} orbital filled with one electron (photo-induced electron) to form a relatively stable Co–N bond, generating one σ bonding orbital occupied by paired electrons and one empty antibonding orbital (σ*). The formation of this relatively stable Co–N bond leads to changes in the coordination configuration of Co and the Co-3d orbital energy level splitting (Fig. S69†), which may cause tiny alterations in the structure or the local electron/hole concentrations in InTCP–Co. Therefore, InTCP–Co exhibits a response to NO_2.

As a representative analyte with paired electrons in its free states, NH_3 was chosen as a comparison to probe the orbital hybridization interaction with InTCP–Co. As shown in Fig. 5c, although hybridization between Co-3d_{z^2} and N-2s2p_z hybrid orbitals is observed, the interaction is weak due to the antibonding characteristics of the majority of the 3d_{z^2}–2s2p_z hybrid in the COHP curve. In addition, the Fermi level falls in the antibonding region of the 3d_{z^2}–2s2p_z hybrid orbitals according to the COHP analysis. This is mainly caused by the fact that the N-2s2p_z hybrid orbital occupied by two electrons (lone pair electrons) in NH_3 hybridizes with the Co-3d_{z^2} orbital with one electron (light-generated electron) to form one σ bonding orbital occupied by paired electrons and one σ antibonding orbital (σ*) occupied by one electron (Fig. 5d). In comparison to NO_2, the weak interaction between NH_3 and InTCP–Co is likely to cause minute changes in the structure or the local electron/hole concentrations in InTCP–Co. Consequently, InTCP–Co exhibits low response values for the measured analytes with all paired electrons in their molecules in their free states.

Despite the presence of an unpaired electron in NO in its free state, it occupies the π_{px} antibonding orbital (π^*_{px}). Notoriously, the π^*_{px} orbital is antisymmetric, which mismatches with the symmetrical Co-3d_{z^2} orbital in InTCP–Co (Fig. 5e and f). As a result, the orbital hybridization interaction between the symmetrical Co-3d_{z^2} orbital and π^*_{px} orbital is extremely weak. Although the symmetry of the π^*_{px} orbital matches the degenerate Co-3d_{xz} and Co-3d_{yz} orbitals, the orbital hybridization interaction between π^*_{px} and Co-3d_{xz}/Co-3d_{yz} is also weak. This is due to the fact that the Co-3d_{xz} and Co-3d_{yz} orbitals each are occupied by two electrons, which leads to an unstable Co–N bond accompanied by a π^*_{px} orbital occupied by one electron (Fig. 5e and f). Similarly, the Co-3d_{z^2} orbital occupied by one electron (photogenerated electron) also forms an unstable Co–N bond with the σ bonding orbital (σ_{pz-pz}) or σ antibonding orbital (σ^*_{2s}). In brief, the orbital interaction between NO and InTCP–Co is weak. Compared with NO_2, NO does not cause significant changes in the structure or local electron/hole concentrations, resulting in a lower response value to NO than that to NO_2 in InTCP–Co.

Based on the experimental results and theoretical calculations, a potential mechanism is proposed to explain the exceptional selective sensitivity of InTCP–Co to NO_2 under visible light irradiation. Specifically, when InTCP–Co sensors were exposed to the NO_2 atmosphere, NO_2 was adsorbed on the Co site of InTCP–Co in a V-shaped fashion. The N-2s2p$_z$ hybrid orbital (filled by one unpaired electron) in NO_2 hybridizes with the Co-3d$_{z^2}$ orbital (occupied by one photogenerated electron with the beta spin state) to form a relatively stable Co–N bond, leading to a change in the coordination configuration of Co and the splitting of the Co-3d orbital energy level. These changes might cause alterations in the structure or local electron/hole concentrations in InTCP–Co, resulting in a conductivity variation and generating a sensing response to NO_2. When NO_2 is removed from the test environment, the amount of NO_2 attached to InTCP–Co gradually decreases, which could revert the coordination configuration of Co and the splitting of the Co-3d orbital energy levels to their original states, then causing the local electron/hole concentrations in InTCP–Co to return to their original states. Thereby, the current recovers. With the assistance of visible light irradiation, the photogenerated electrons can transition to the unoccupied Co-3d$_{z^2}$ orbitals, enhancing the orbital interaction between NO_2 and InTCP–Co. Therefore, compared to the conditions without light, the response value to NO_2 could be improved under visible light illumination. Among the examined combinations of FeTCP–M and InTCP–M (M = Fe, Co, Ni and Zn), InTCP–Co exhibits a higher response value and excellent selectivity to NO_2, which is primarily attributed to superior electron spin state matching, increased orbital overlap, improved orbital symmetry compatibility between the N-2s2p$_z$ hybrid orbital of NO_2 and Co-3d$_{z^2}$ orbital, more favourable electron transfer paths and the promotion of the photoelectrons.

Conclusions

In summary, we have fabricated a series of reversible chemiresistive gas sensors using MOFs featuring metalloporphyrin facets aligned by a periodic array of In/Fe–oxo pillars, FeTCP–M and InTCP–M (M = Fe, Co, Ni and Zn). The response of the catechol–metalloporphyrin scaffolds to NO_2 has been investigated under visible light excitation, and we found that it could be modulated by varying the metal species individually coordinated in porphyrin centers and with catechol groups. Among them, InTCP–Co reveals the highest response and selectivity toward NO_2 under visible light illumination, with an experimental detection limit as low as 40 ppb. Both the experimental results and theoretical calculations reveal that the excellent response performance of InTCP–Co to NO_2 could be ascribed to multiple factors, including the better matching of electron spin state and orbital symmetry, the higher orbital overlap between the N-2s2p$_z$ hybrid orbital of NO_2 and Co-3d$_{z^2}$ orbital, and the more favorable electron transfer pathway in InTCP–Co. This work has provided a new perspective for the design of high-performance chemiresistive gas sensor by regulating the transfer route of charge carriers, electron spin states, orbital overlap and orbital symmetry of analytes and sensitive substances.

Methods

Syntheses of FeTCP–M (M = Fe, Co, Ni and Zn)[40]

$FeCl_2$ (0.075 mmol, 0.0095 g), 3,4-TDHPP–M (0.075 mmol, 0.0597 g, 0.0599 g, 0.0599 g, and 0.0604 g for M = Fe, Co, Ni and Zn, respectively), *N*,*N*-dimethylformamide (DMF, 3.0 mL), water (0.5 mL) and methanol (0.5 mL) were mixed in a 23 mL Teflon-lined stainless steel container and then heated to 140 °C for 4 days. After cooling to room temperature, brown crystal samples were obtained after washing with methanol and drying, named FeTCP–M (M = Fe, Co, Ni and Zn), respectively.

Syntheses of InTCP–M (M = Fe, Co, Ni and Zn)[40]

$In(NO_3)_3 \cdot 4.5H_2O$ (0.075 mmol, 0.0286 g), 3,4-TDHPP–M (0.075 mmol, 0.0597 g, 0.0599 g, 0.0599 g, and 0.0604 g for M = Fe, Co, Ni and Zn, respectively), water (1.0 mL) and DMF (3.0 mL) were mixed in a 23 mL Teflon-lined stainless steel container and then heated to 140 °C for 4 days. After cooling to room temperature, brown crystal samples were obtained after washing with methanol and drying, named InTCP–M (M = Fe, Co, Ni and Zn), respectively.

Fabrication of sensor devices

The ground sample was mixed with moderate isopropanol to form paste. Then the paste was coated on the interdigital electrodes of the sensor substrates (Fig. S13a†). Then the coated sensors were placed in a vacuum oven at 60 °C for 12 h to remove isopropanol.

Gas sensing test

The gas sensing characterization was carried out on a home-made system (Fig. S13b†) which was reported in the previous work.[62] In the gas sensing test, the light source was a 300 W Xe lamp with a 420 nm cutoff filter and the light intensity can be modulated by adjusting the current. The current was 12 mA and the distance between the gas sensor and light source was 8 cm in this work. The current was recorded in real-time using a source meter (Keithley 2602B) and the bias voltage of the device was 5 V during the gas sensing test. The gas (air and the target gas are diluted in the air and NO is diluted in N_2 because NO is easily oxidized in the air) flow rate was controlled at 600 mL min^{-1} which was monitored using mass flow controllers (CS-200C, Beijing Sevenstar Qualiflow Electronic Equipment Manufacturing Co. Ltd, China). The analytical gas was introduced into a quartz tube and the concentration was obtained by controlling the flow ratio of analytical gas and air. The response value (R) of the target gas is defined as:

$$R = \frac{I_g - I_0}{I_0}$$

where I_g is the current of the fabricated sensor in the target gas and I_0 is the current of the fabricated sensor in the air. The response or recovery time is expressed as the time required to reach 90% of the maximum current value change.

In situ diffuse reflectance infrared Fourier transform (DRIFT) spectrum

A Nicolet 6700 FT-IR spectrometer with an MCT/A detector cooled using liquid nitrogen was employed to record the DRIFTS spectra. The background of DRIFTS spectra was obtained with InTCP–Co in synthetic air (79% nitrogen, 21% oxygen). The time-resolved DRIFTS spectra of NO_2 adsorption (100 ppm NO_2 in synthetic air) were recorded under the same conditions as the background test. All spectra were collected with a resolution of 4 cm^{-1} by scanning 128 times.

Density functional theory (DFT)-based calculations

The DFT calculations and structure optimization of FeTCP–M and InTCP–M (M = Fe, Co, Ni and Zn) were carried out using the Vienna *ab initio* simulation package (VASP)[63,64] based on the projected augmented wave (PAW) pseudopotential method.[65–67] The generalized gradient approximation (GGA) of the exchange-correlation functional with the Perdew–Burke–Ernzerhof (PBE) functional was introduced.[68] The Brillouin-zone integration was sampled using a (1 × 1 × 1) Monkhorst–Pack mesh[69] and the kinetic energy cutoff for the plane-wave expansion was set to 400 eV in the simulations. The *K*-points were improved in the calculations of the crystal orbital Hamilton population (COHP). All of the atoms in the structures were fully relaxed to the ground state. The vdW-DF method was employed to solve the spin-polarized effect and the effect of dispersion. The energy convergence changes and maximum force for geometric optimization were set to 0.02 eV $Å^{-1}$ and 10^{-6} eV, respectively. A (1 × 1 × 1) unit cell as a model was constructed in the DFT calculations. The adsorption energies (E_{ads}) of different analytes on InTCP–Co are defined as $E_{ads} = E_{A+B} - E_A - E_B$, where E_{A+B}, E_A, and E_B are the total DFT energies of analytes adsorbed on InTCP–Co, InTCP–Co and isolated analyte molecules, respectively.

Author contributions

E.-X. C. and Q. L. conceived and designed the idea. E.-X. C. carried out the experiments and characterization, L. H. provided help for modifying pictures in the article, M. Q. performed DFT calculations and analysis, Y. Z. provided resources for DFT, Y. S. performed gas adsorption measurements, W.-H. L., J.-Z. X. and J. C. provided help for gas sensing measurements, G. X. provided resources for gas sensing measurements, and E.-X. C., G. X. and Q. L. wrote the manuscript. All the authors discussed the results and commented on the manuscript.

Conflicts of interest

There are no conflicts to declare.

Acknowledgements

This work was financially supported by the National Science Foundation of China (22201283, 22325109, 22171263, 62227815, 22269009, and 21773030), the National Key Research and Development Project (2022YFA1503900), the National Science Foundation of Fujian Province (2022J05090, 2022T3008, and 2021J02017), the Scientific Research and Equipment Development Project of CAS (YJKYQ20210024), Fujian Science & Technology Innovation Laboratory for Optoelectronic Information of China (2021ZR138), the Open Project Program of the State Key Laboratory of Photocatalysis on Energy and Environment (SKLPEE-KF202204), Fuzhou University and the Self-Deployment Project Research Program of Haixi Institutes, Chinese Academy of Sciences (CXZX-2022-GH09).

Notes and references

1 D. B. Cao, X. Liu, J. P. Lewis, W. Guo and X. Wen, *Angew. Chem., Int. Ed.*, 2022, **61**, e202202751.
2 Q. K. Li, X. F. Li, G. Zhang and J. Jiang, *J. Am. Chem. Soc.*, 2018, **140**, 15149–15152.
3 L.-Y. Zhu, L.-X. Ou, L.-W. Mao, X.-Y. Wu, Y.-P. Liu and H.-L. Lu, *Nano-Micro Lett.*, 2023, **15**, 89.
4 X. Yang, Y. Deng, H. Yang, Y. Liao, X. Cheng, Y. Zou, L. Wu and Y. Deng, *Adv. Sci.*, 2022, **10**, e2204810.
5 O. Lupan, N. Ababii, D. Santos-Carballal, M.-I. Terasa, N. Magariu, D. Zappa, E. Comini, T. Pauporté, L. Siebert, F. Faupel, A. Vahl, S. Hansen, N. H. de Leeuw and R. Adelung, *Nano Energy*, 2021, **88**, 106241.
6 Y. Kim, S. Lee, J. G. Song, K. Y. Ko, W. J. Woo, S. W. Lee, M. Park, H. Lee, Z. Lee, H. Choi, W.-H. Kim, J. Park and H. Kim, *Adv. Funct. Mater.*, 2020, **30**, 2003360.
7 X. Geng, D. Liu, C. C. Hewa-Rahinduwage, S. L. Brock and L. Luo, *Acc. Chem. Res.*, 2023, **56**, 1087–1096.
8 G. Shao, O. Ovsianytskyi, M. F. Bekheet and A. Gurlo, *Chem. Commun.*, 2020, **56**, 450–453.
9 H. Lim, H. Kwon, H. Kang, J. E. Jang and H.-J. Kwon, *Nat. Commun.*, 2023, **14**, 3114.
10 X. Liu, W. Zheng, R. Kumar, M. Kumar and J. Zhang, *Coord. Chem. Rev.*, 2022, **462**, 214517.
11 C. Zhu, Y. Xu, T. Zhou, L. Liu, Q. Chen, B. Gao and T. Zhang, *Sens. Actuators, B*, 2022, **365**, 131928.
12 K. Wang, Y. Li, L.-H. Xie, X. Li and J.-R. Li, *Chem. Soc. Rev.*, 2022, **51**, 6417–6441.
13 Y.-S. Wei, M. Zhang, R. Zou and Q. Xu, *Chem. Rev.*, 2020, **120**, 12089–12174.
14 Z. Ji, T. Li and O. M. Yaghi, *Science*, 2020, **369**, 674–780.
15 H. Lyu, O. I. Chen, N. Hanikel, M. I. Hossain, R. W. Flaig, X. Pei, A. Amin, M. D. Doherty, R. K. Impastato, T. G. Glover, D. R. Moore and O. M. Yaghi, *J. Am. Chem. Soc.*, 2022, **144**, 2387–2396.
16 W. Zhang, J. Wu, W. Shi, P. Qin, W. Lang, X. Zhang, Z. Gu, H. Li, Y. Fan, Y. Shen, S. Zhang, Z. Liu, Y. Fu, W. Zhang and F. Huo, *Adv. Mater.*, 2023, **35**, e2303216.
17 L. He, Y.-J. Guo, Y.-H. Xiao, E.-X. Chen, M.-B. Luo, Z.-H. Li and Q. Lin, *CCS Chem.*, 2022, **4**, 2286–2293.
18 E.-X. Chen, H. R. Fu, R. Lin, Y. X. Tan and J. Zhang, *ACS Appl. Mater. Interfaces*, 2014, **6**, 22871–22875.
19 E.-X. Chen, H. Yang and J. Zhang, *Inorg. Chem.*, 2014, **53**, 5411–5413.

20 H.-Y. Li, S. N. Zhao, S.-Q. Zang and J. Li, *Chem. Soc. Rev.*, 2020, **49**, 6364–6401.
21 M.-S. Yao, W.-H. Li and G. Xu, *Coord. Chem. Rev.*, 2021, **426**, 213479.
22 W.-T. Koo, J.-S. Jang and I.-D. Kim, *Chem*, 2019, **5**, 1938–1963.
23 Z. Meng, A. Aykanat and K. A. Mirica, *J. Am. Chem. Soc.*, 2019, **141**, 2046–2053.
24 H.-Z. Li, Y. Pan, Q. Li, Q. Lin, D. Lin, F. Wang, G. Xu and J. Zhang, *J. Mater. Chem. A*, 2023, **11**, 965–971.
25 Y.-M. Jo, Y. K. Jo, J.-H. Lee, H. W. Jang, I. S. Hwang and D. J. Yoo, *Adv. Mater.*, 2023, **35**, e2206842.
26 M. E. DMello, N. G. Sundaram, A. Singh, A. K. Singh and S. B. Kalidindi, *Chem. Commun.*, 2019, **55**, 349–352.
27 M. G. Campbell, D. Sheberla, S. F. Liu, T. M. Swager and M. Dincă, *Angew. Chem., Int. Ed.*, 2015, **54**, 4349–4352.
28 X.-C. Zhou, C. Liu, J. Su, Y.-F. Liu, Z. Mu, Y. Sun, Z.-M. Yang, S. Yuan, M. Ding and J.-L. Zuo, *Angew. Chem., Int. Ed.*, 2023, **62**, e202211850.
29 M.-S. Yao, J.-W. Xiu, Q.-Q. Huang, W.-H. Li, W.-W. Wu, A.-Q. Wu, L.-A. Cao, W.-H. Deng, G.-E. Wang and G. Xu, *Angew. Chem., Int. Ed.*, 2019, **58**, 14915–14919.
30 T. K. Townsend, E. M. Sabio, N. D. Browning and F. E. Osterloh, *Energy Environ. Sci.*, 2011, **4**, 4270–4275.
31 S. M. Majhi, S. T. Navale, A. Mirzaei, H. W. Kim and S. S. Kim, *Inorg. Chem. Front.*, 2023, **10**, 3428–3467.
32 R. Tian, Z. Gao, G. Chen, H. Guan, C. Dong and E. Comini, *Sens. Actuators, B*, 2023, **383**, 133584.
33 D. Wang, C. Han, C. Zheng, H. Fang, D. Xu and H. Zhao, *Sens. Actuators, B*, 2023, **387**, 133833.
34 F. Lei, Y. Sun, K. Liu, S. Gao, L. Liang, B. Pan and Y. Xie, *J. Am. Chem. Soc.*, 2014, **136**, 6826–6829.
35 N. Pattanayak, P. Panda and S. Parida, *Ceram. Int.*, 2022, **48**, 7636–7642.
36 R. Singh and A. Mukherjee, *ACS Catal.*, 2019, **9**, 3604–3617.
37 Z. W. Hao, M. M. Dong, R. Q. Zhang, C. K. Wang and X. X. Fu, *Phys. Chem. Chem. Phys.*, 2021, **23**, 11852–11862.
38 H. Lee, H. Park, D. Y. Ryu and W. D. Jang, *Chem. Soc. Rev.*, 2023, **52**, 1947–1974.
39 Y.-X. Li, J. Li, H.-B. Zeng, X.-J. Zhang, S. Cosnier and D. Shan, *Anal. Chem.*, 2023, **95**, 3493–3498.
40 E.-X. Chen, M. Qiu, Y.-F. Zhang, L. He, Y.-Y. Sun, H.-L. Zheng, X. Wu, J. Zhang and Q. Lin, *Angew. Chem., Int. Ed.*, 2022, **61**, e202111622.
41 M. G. Campbell, S. F. Liu, T. M. Swager and M. Dincă, *J. Am. Chem. Soc.*, 2015, **137**, 13780–13783.
42 D. Sheberla, L. Sun, M. A. Blood-Forsythe, S. Er, C. R. Wade, C. K. Brozek, A. Aspuru-Guzik and M. Dincă, *J. Am. Chem. Soc.*, 2014, **136**, 8859–8862.
43 Y. S. Bae, C. Y. Lee, K. C. Kim, O. K. Farha, P. Nickias, J. T. Hupp, S. T. Nguyen and R. Q. Snurr, *Angew. Chem., Int. Ed.*, 2012, **51**, 1857–1860.
44 K. Lee, W. C. Isley, A. L. Dzubak, P. Verma, S. J. Stoneburner, L. C. Lin, J. D. Howe, E. D. Bloch, D. A. Reed, M. R. Hudson, C. M. Brown, J. R. Long, J. B. Neaton, B. Smit, C. J. Cramer, D. G. Truhlar and L. Gagliardi, *J. Am. Chem. Soc.*, 2014, **136**, 698–704.
45 H. Nishihara, M. Ohwada, T. Kamimura, M. Nishimura, H. Tanaka, S. Hiraide, M. T. Miyahara, K. Ariga, Q. Ji, J. Maruyama and F. Tani, *Chem. Commun.*, 2018, **54**, 7822–7825.
46 E. Nikoloudakis, I. López-Duarte, G. Charalambidis, K. Ladomenou, M. Ince and A. G. Coutsolelos, *Chem. Soc. Rev.*, 2022, **51**, 6965–7045.
47 J. Ding, X. Guan, J. Lv, X. Chen, Y. Zhang, H. Li, D. Zhang, S. Qiu, H. L. Jiang and Q. Fang, *J. Am. Chem. Soc.*, 2023, **145**, 3248–3254.
48 E. Ozensoy, C. H. F. Peden and J. Szanyi, *J. Phys. Chem. B*, 2005, **109**, 15977–15984.
49 B. Sun, H. Lv, Z. Liu, J. Wang, X. Bai, Y. Zhang, J. Chen, K. Kan and K. Shi, *J. Mater. Chem. A*, 2021, **9**, 6335–6344.
50 X. Han, H. G. W. Godfrey, L. Briggs, A. J. Davies, Y. Cheng, L. L. Daemen, A. M. Sheveleva, F. Tuna, E. J. L. McInnes, J. Sun, C. Drathen, M. W. George, A. J. Ramirez-Cuesta, K. M. Thomas, S. Yang and M. Schröder, *Nat. Mater.*, 2018, **17**, 691–696.
51 L. Zhang, L. Shi, L. Huang, J. Zhang, R. Gao and D. Zhang, *ACS Catal.*, 2014, **4**, 1753–1763.
52 Q. Zhao, B. Chen, J. Li, X. Wang, M. Crocker and C. Shi, *Appl. Catal., B*, 2020, **277**, 119215.
53 J. Abdul Nasir, J. Guan, T. W. Keal, A. W. Desmoutier, Y. Lu, A. M. Beale, C. R. A. Catlow and A. A. Sokol, *J. Am. Chem. Soc.*, 2023, **145**, 247–259.
54 F. Wang, P. Wang, T. Lan, Y. Shen, W. Ren and D. Zhang, *ACS Catal.*, 2022, **12**, 7622–7632.
55 M. Diaz-Lopez, S. A. Guda and Y. Joly, *J. Phys. Chem. A*, 2020, **124**, 6111–6118.
56 P. C. Müller, C. Ertural, J. Hempelmann and R. Dronskowski, *J. Phys. Chem. C*, 2021, **125**, 7959–7970.
57 S. Maintz, V. L. Deringer, A. L. Tchougréeff and R. Dronskowski, *J. Comput. Chem.*, 2016, **37**, 1030–1035.
58 R. Dronskowski and P. E. Blöchl, *J. Phys. Chem. Lett.*, 1993, **97**, 8617–8624.
59 V. L. Deringer, A. L. Tchougréeff and R. Dronskowski, *J. Phys. Chem. A*, 2011, **115**, 5461–5466.
60 B. D. Dunnington and J. R. Schmidt, *J. Chem. Theory Comput.*, 2012, **8**, 1902–1911.
61 E. D. Glendening, C. R. Landis and F. Weinhold, *J. Comput. Chem.*, 2019, **40**, 2234–2241.
62 M.-S. Yao, W.-X. Tang, G.-E. Wang, B. Nath and G. Xu, *Adv. Mater.*, 2016, **28**, 5229–5234.
63 G. Kresse and J. Hafner, *Phys. Rev. B: Condens. Matter Mater. Phys.*, 1993, **47**, 558–561.
64 G. Kresse and J. Hafner, *Phys. Rev. B: Condens. Matter Mater. Phys.*, 1993, **48**, 13115–13118.
65 P. E. Blöchl, *Phys. Rev. B: Condens. Matter Mater. Phys.*, 1994, **50**, 17953–17979.
66 G. Kresse and D. Joubert, *Phys. Rev. B: Condens. Matter Mater. Phys.*, 1999, **59**, 1758–1775.
67 J. Hafner, *J. Comput. Chem.*, 2008, **29**, 2044–2078.
68 J. P. Perdew, K. Burke and M. Ernzerhof, *Phys. Rev. Lett.*, 1996, **77**, 3865–3868.
69 H. J. Monkhorst and J. D. Pack, *Phys. Rev. B: Solid State*, 1976, **13**, 5188–5192.